PAPER

Modeling of internal conversion in photoexcited conjugated molecular donors used in organic photovoltaics†

N. Oldani,[a] S. Tretiak,*[b] G. Bazan[c] and S. Fernandez-Alberti*[a]

Using the Non-Adiabatic Excited States Molecular Dynamics (NA-ESMD) approach, we investigate the ultrafast electronic relaxation in a recently synthesized small molecule donor, p-DTS(PTTh$_2$)$_2$, which belongs to the dithienosilole-pyridylthiadiazole family of chromophores. In combination with the PC$_{70}$BM acceptor, p-DTS(PTTh$_2$)$_2$ can be used to fabricate high efficiency bulk heterojunction organic solar cells. After photoexcitation to its broad high-energy peak in the 3–4 eV range, associated with multiple excited states, p-DTS(PTTh$_2$)$_2$ undergoes efficient ultrafast internal conversion to its lowest excited state. During this process, about 1–2 eV electronic energy transfers to the vibrational degrees of freedom leading to rapid heating of the molecule. Nevertheless, our simulations do not detect possible bond-breaking or decomposition of the system. This suggests minimal intra-molecular photodamage after photoexcitation to high-energy states in the 3–4 eV region. Calculated radiationless deactivation mainly consists of a sequential mechanism that involves electronic transitions between the current transient state and the corresponding state directly below in energy. Changes in the density of states along the relaxation process lead to pronounced variations and time-dependence of the accumulated populations of the different intermediate electronic excited states. Visualization of the electronic transition density during internal conversion reveals spatial intramolecular delocalization of electronic excitation from the thiophene moieties to the entire chromophore. Finally, our analysis of non-adiabatic coupling vectors suggests characteristic vibrational degrees of freedom coupled to the electronic system during various stages of non-radiative relaxation.

Broader context

Considerable world-wide effort in both industry and academia has been focused on developing organic photovoltaic (OPV) cell and module technologies, which can potentially meet multiple requirements for solar energy conversion. Here, power conversion efficiencies (PCEs) exceeding 10% have been achieved in the case of bulk-heterojunction (BHJ) solar cell structures. These values of PCE are still below those corresponding to inorganic solar cells but steady improvements have been made. In recent years, small molecules have emerged as favorable novel organic compounds owing to their exceptional light-harvesting capacity and efficient charge transport. For example, solar cells fabricated using a recently synthesized molecular donor p-DTS(PTTh$_2$)$_2$ exhibited the highest record value of 6.7% for the PCE, this revealing the potential of small donor molecular materials. The performance of such OPV devices depends on a complex interplay of charge and energy transfer timescales competing with radiative and non-radiative relaxations, and various energy-loss mechanisms. Subsequently, design of new molecules involves optimization of many important parameters including detailed understanding of excited state dynamics relevant to charge transfer reactions in solar cells, as well as insights into the underlying vibrational/conformational dynamics and mechanisms of photo-degradation of materials. Here we present computational investigation of internal conversion in the p-DTS(PTTh$_2$)$_2$ molecule discovering details of its complex coupled electron-vibrational dynamics, constituting a primary relaxation step in the photoexcited material of the solar cell followed by exciton diffusion. By deciphering all loss pathways and rapid internal conversion processes, our study delivers critical knowledge necessary for future improvements of light-harvesting capabilities in BHJ solar cells based on small donor molecules.

[a]*Universidad Nacional de Quilmes, Roque Saenz Peña 352, B1876BXD Bernal, Argentina. E-mail: sfalberti@gmail.com*

[b]*Theoretical Division, Center for Nonlinear Studies (CNLS), and Center for Integrated Nanotechnologies (CINT), Los Alamos National Laboratory, Los Alamos, NM 87545, USA. E-mail: serg@lanl.gov*

[c]*Center for Polymers and Organic Solids, Departments of Chemistry & Biochemistry and Materials, University of California, Santa Barbara, California 93106, USA*

I. Introduction

Light harvesting from the sun can be considered as one of the most important ways to address the growing global needs for inexpensive, clean and renewable energy resources. Photovoltaic technology is one of the most promising approaches to reach this goal. It necessitates development of efficient and inexpensive solar cells (also called photovoltaic cells), which are

This journal is © The Royal Society of Chemistry 2014

Energy Environ. Sci., 2014, **7**, 1175–1184 | **1175**

devices that convert the energy of light directly into electricity by the photovoltaic effect. Within this context, organic solar cells have great potential since organic materials have many advantages compared to traditional inorganic semiconductors: low cost processing (*e.g.*, ink-jet printing), an established variety of solution-based synthetic methods, sustainability, and plastic processing ability.[1,2] The extensive development in the field of organic photovoltaic (OPV) research has proved that these devices provide cost effective energy generating sources.[1–11] The vast majority of these studies have been focused on organic bulk heterojunction (BHJ) solar cells[12] consisting of a blend of conjugated polymers (acting as donors) and fullerene molecules (acting as acceptors) like the phenyl-C61-butyric acid methyl ester (PCBM).[11,13–17] Among the growing number of conjugated polymers and molecules serving as optical absorbers in the visible range of solar radiation, we can mention those based on poly(3-hexylthiophene), fluorene, phenylene[1,13] and donor–acceptor–donor co-monomers in alternating copolymers.[14]

The efficient photoinduced donor–acceptor electron transfer that takes place in BHJ solar cells is in competition with radiative or nonradiative relaxations of the excess of energy initially localized in the donor molecule. The power conversion efficiency (PCE) of the device[18] depends on the relative time scale of these processes. Over the years the PCE in OPV technology has steadily grown[19] fueled by a wide range of research efforts worldwide.[9,20–25] Recently PCEs as high as 11% in single junction cells and 12% in tandem cells have been reported[19,26] overcoming an important 10% threshold. While these values of PCE are significantly less than those corresponding to inorganic solar cells, their steady improvement has awakened strong interest in the potential for OPVs to offer practical, widespread energy production. The key is designing new materials which fulfill multiple parameters necessary for the OPV purpose, such as light harvesting, dealing with loss mechanisms, electron transfer, and transport.

In recent years, small molecule donors have emerged as favorable novel organic compounds for solar cells.[27–30] Small molecules are easier to synthesize and purify than polymers,[31] and can largely fill the need for an n-type component in BHJs. Therefore, they can still produce a photovoltaic effect, forming the so-called solution-processed molecular bulk heterojunction (SMBHJ).[27] As examples of the most successful compounds applied as donors in SMBHJs, we can mention oligothiophenes,[32–36] acenes,[37–40] diketopyrrolopyrroles,[41] push–pull type oligomers,[42] and dye based materials.[43–46]

In the present work, we focus our attention on the photodynamics of the recently synthesized molecular donor *p*-DTS(PTTh$_2$)$_2$ (ref. 47) containing dithienosilole (DTS), pyridylthiadiazole (PT), and thiophene (Th) moieties (see Fig. 1(a)). This light-harvesting small molecule exhibits broad optical absorption from 600 to 800 nm. Its structure consists of an acceptor/donor/acceptor (A/D/A) core with Th$_2$ donor endcapping units that extend the π-conjugation. The PT moieties act as acceptor units due to their high electron affinity and they are linked through the electron rich donor DTS unit. This scheme leads to strong intramolecular charge transfer and broad low-energy optical transitions.[14,48–52] Previous studies have reported
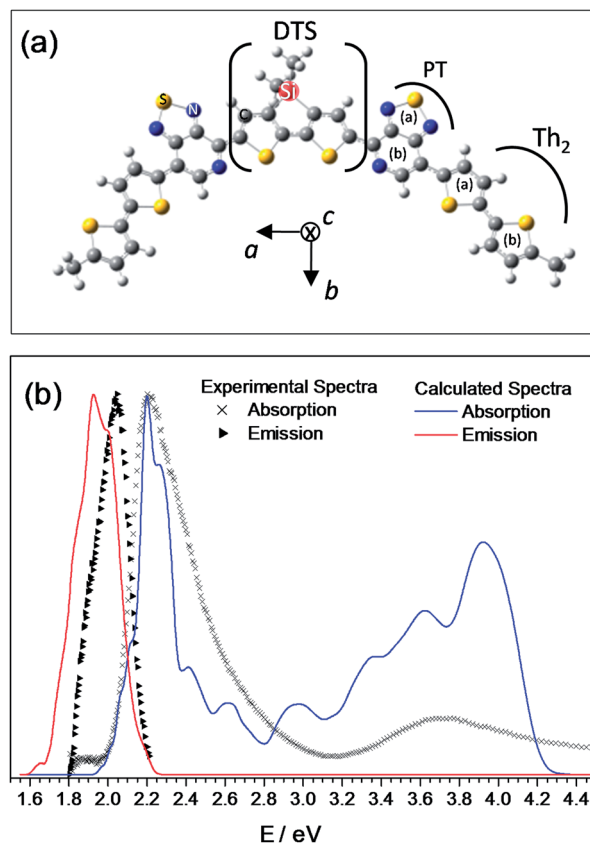

Fig. 1 (a) Chemical structure of the *p*-DTS(PTTh$_2$)$_2$ molecule: DTS is dithienosilole and PT is pyridalthiadiazole; (b) experimental and simulated absorption and emission spectra of the *p*-DTS(PTTh$_2$)$_2$ molecule. The experimental spectrum has been shifted by 0.34 eV.

the highest record value of 6.7% for the PCE of *p*-DTS(PTTh$_2$)$_2$,[53] demonstrating that solar cells fabricated from small donor molecules can compete in performance with those based on polymer donors.

The well-defined structure of *p*-DTS(PTTh$_2$)$_2$ enables the study of its electronic structure properties. In a previous study,[54] the absorption and emission spectra have been characterized using Density Functional Theory (DFT) and time-dependent DFT (TDDFT) approaches. The broad strong low-energy peak (∼2 eV) in the experimental UV-vis absorption spectrum has been attributed to the lowest band-gap S$_0$–S$_1$ transition polarized along the long axis of the molecule, whereas a shoulder on the blue side of the peak has been associated with a second electronic transition whose transition dipole moment is perpendicular to the previous one. At higher energies, the spectrum features a broad peak of lower intensity in the 3–4 eV range that has been associated with multiple excited states. Furthermore, a moderate coupling (63 meV) between the nearest neighbors in the molecular crystal has been reported to occur in the π-stack mediated by a significant transition dipole moment of the lowest excited state. These results suggest the intermolecular exciton transfer rates to be as high as a few hundreds of femtoseconds[54] in the framework of Förster theory. Prior to this intermolecular exciton transport,[54] we expect rapid

1176 | *Energy Environ. Sci.*, 2014, 7, 1175–1184

This journal is © The Royal Society of Chemistry 2014

intramolecular non-radiative relaxation[55] of p-DTS(PTTh$_2$)$_2$ photoexcitation to the first electronic excited state, which is a main subject in the present work.

Specifically, here we study the intramolecular redistribution and relaxation of the excess of electronic energy after photoexcitation of p-DTS(PTTh$_2$)$_2$ to the broad high-energy band in the 3–4 eV range. A detailed description of the p-DTS(PTTh$_2$)$_2$ photodynamics is essential to achieve a comprehensive picture of its exceptional light-harvesting and donor capabilities in BHJ solar cells. Exciton formation, evolution of the transient electronic transition density, and non-radiative decay *via* internal conversion are important processes that can have a significant impact on the performance of the molecule as donor in SMBHJs. We make use of our previously developed non-adiabatic excited state molecular dynamics (NA-ESMD) framework[56,57] suitable for dealing with photodynamics in extended conjugated molecules consisting of hundreds of atoms on time scales of tens of picoseconds. The NA-ESMD method uses calculating *on the fly* excited-state energies, gradients and respective non-adiabatic coupling terms. It has been previously successfully applied to model non-radiative photoinduced dynamics in several conjugated oligomers.[55,57–60]

The article is organized as follows: in Section II we provide a brief overview of the NA-ESMD approach, electronic transition density calculations, and computational details related to the simulation of the photoexcitation and subsequent non-adiabatic excited-state dynamics of the p-DTS(PTTh$_2$)$_2$ molecule. In Section III we present and discuss our results. Finally, conclusions are given in Section IV.

II.   Methods

A.   The NA-ESMD methodology

The NA-ESMD[56,61,62] method has been developed to simulate photoinduced dynamics of extended conjugated molecules involving multiple coupled electronic excited states. It is a *direct* nonadiabatic molecular dynamics simulation method[63] that combines the *surface hopping* molecular dynamics with quantum transition (MDQT)[64–66] approach with "*on the fly*" analytical calculations of excited state energies,[67–69] gradients,[56,70,71] and non-adiabatic coupling[56,72–74] terms. In particular, non-adiabatic coupling vector $\mathbf{d}_{\alpha\beta} = \langle \phi_\alpha(\mathbf{r};\ \mathbf{R}) | \nabla_{\mathbf{R}} \phi_\beta(\mathbf{r};\ \mathbf{R}) \rangle$ between the α and β electronic excited states (where ϕ_α (ϕ_β) are the adiabatic Hamiltonian eigenstates and $\mathbf{r}$ and $\mathbf{R}$ are the electronic and nuclear coordinates) drives quantum transitions: its magnitude defines the probability of the transition whereas its direction corresponds to the direction of the dominant driving force for nuclear motion in regions of strong non-adiabatic couplings.[66,75–78] All these quantities are calculated using the collective electron oscillator (CEO) method[79–82] applied at the Austin Model 1 (AM1)[83] semiempirical level in combination with the configuration interaction singles (CIS) formalism to describe correlated excited states. The NA-ESMD code has been extensively optimized in order to permit the description of photoinduced dynamics in extended conjugated molecular systems consisting of hundreds of atoms on the time scales of tens of picoseconds. Its implementation of the MDQT

method combines excited-state methodologies (Davidson diagonalization, analytical gradients and nonadiabatic couplings) with the synergy of the velocity Verlet and Runge–Kutta propagators used to propagate nuclei and electrons. The potential existence of trivial unavoided crossings between non-interacting adiabatic states has been followed and treated using a novel numerical procedure based on the Min-Cost algorithm.[60] Detailed discussion about the NA-ESMD implementation, advantages, and testing parameters can be found elsewhere.[57]

B.   Electronic transition density

During photoexcited dynamics, the intramolecular electronic energy redistribution is followed using the time-dependent localization of the electronic transition density for the current state. The CEO approach[84,85] calculates transition density matrices $(\rho^{g\alpha})_{nm} \equiv \langle \phi_\alpha(\mathbf{r};\ \mathbf{R}(t)) | c_m^+ c_n | \phi_g(\mathbf{r};\ \mathbf{R}(t)) \rangle$ (denoted as *electronic normal modes*) using the ground-state density matrix. Here $c_m^+(c_n)$ represents the creation (annihilation) operator; and indices n and m refer to atomic orbital (AO) basis functions. Changes in the distribution of the electronic density induced by photoexcitation from the ground state g to an excited electronic α state are followed through the diagonal elements of $(\rho^{g\alpha})_{nn}$ (ref. 86) with the required normalization condition $\sum_{n,m} (\rho^{g\alpha})_{nm}^2 = 1$ according to the CIS approximation.[69] Therefore, the fraction of the transition density localized on the different moieties of the p-DTS(PTTh$_2$)$_2$ molecule can be calculated as

$$(\rho^{g\alpha})_X^2 = \sum_{n_A m_A} (\rho^{g\alpha})_{n_A m_A}^2 + \frac{1}{2} \sum_{n_B m_B} (\rho^{g\alpha})_{n_B m_B}^2 \tag{1}$$

where the index A runs over all atoms localized in the X-moiety (X = DTS, PT, Th) and the index B runs over atoms localized in between these units. We can thereby define the atomic participation number[87,88] of the current electronic transition density as

$$P_{at}(t) = \left(\sum_{j=1}^{N} \left((\rho^{g\alpha})_j^2 \right)^2 \right)^{-1} \tag{2}$$

with

$$(\rho^{g\alpha})_j^2 = \sum_{n_j m_j}^{N_{AO}^j} (\rho^{g\alpha})_{n_j m_j}^2 \tag{3}$$

where N is the number of heavy atoms (C, N, S, and Si) in the molecule and N_{AO}^j is the number of atomic orbital (AO) basis functions of the jth atom. Values of $\mathbf{P}_{at}(t) \approx N$ mean that the excitation is completely delocalized over all atoms, while values of $\mathbf{P}_{at}(t) \approx 1$ correspond to excitations involving a single atom. In the same way, if we divide the p-DTS(PTTh$_2$)$_2$ molecule into two equivalent L (left) and R (right) branches, we can define the branch participation number as

$$P_{branch}(t) = \left(\left((\rho^{g\alpha})_L^2 \right)^2 + \left((\rho^{g\alpha})_R^2 \right)^2 \right)^{-1} \tag{4}$$

This journal is © The Royal Society of Chemistry 2014

Energy Environ. Sci., 2014, **7**, 1175–1184 | **1177**

with $(\rho^{g\alpha})_L{}^2$ and $(\rho^{g\alpha})_R{}^2$ being the fractions of the transition density localized in the left and right branches defined in the same manner as eqn (1). In this case, $\mathbf{P}_{branch}(t) \approx 2$ corresponds to transitions equally distributed between the two sides of the molecule, and $\mathbf{P}_{branch}(t) \approx 1$ corresponds to transitions localized on only one side.

C. Molecular dynamics simulations

The p-DTS(PTTh$_2$)$_2$ molecular system used in the NA-ESMD simulations is depicted in Fig. 1(a). 1 ns of an equilibrated ground state molecular dynamics simulation at 300 K using the Langevin friction coefficient γ of 2.0 ps^{-1} has been employed to generate the required conformational sampling of initial positions and momenta for the subsequent NA-ESMD modeling. The initial excited state was chosen according to a Frank–Condon window defined as

$$g_\alpha(\mathbf{r}, \mathbf{R}) = \exp[-T^2(E_{laser} - \Omega_\alpha)^2] \tag{5}$$

where E_{laser}, expressed in units of fs^{-1} as well as Ω_α, represents the energy of a laser centred at 3.65 eV (400 nm) that corresponds to the middle of the broad high-energy band in the 3–4 eV range of the absorption spectrum. A Gaussian laser pulse, $f(t) = \exp(-t^2/2T^2)$, has been considered with $T^2 = 42.5$ fs corresponding to a FWHM (Full Width at Half Maximum) of 100 fs. Since the excitation band is associated with multiple excited states,[54] the initial excited state is selected according to the relative values of the $g_\alpha(\mathbf{r}, \mathbf{R})$ weighted by the oscillator strengths of each state α.

The AM1/CIS level of theory has been used to calculate the energies, gradients, and nonadiabatic coupling terms required during the NA-ESMD simulations. Forty electronic states and their corresponding nonadiabatic couplings were included in the simulations. 400 NA-ESMD trajectories of 500 fs duration at 300 K (room temperature) were propagated in order to obtain reasonable statistics of photoexcited wavepacket evolution. A classical time step of 0.5 fs (0.1 fs) has been used for nuclei propagation in ground (non-adiabatic excited) state dynamics. Besides, a quantum time step of 0.025 fs has been used to propagate the electronic degrees of freedom during the NA-ESMD. In order to identify and deal with trivial unavoided crossings, the quantum time step was further reduced by a factor of 40 in the vicinity of such crossings. More details concerning the NA-ESMD implementation and parameters can be found elsewhere.[56,57,60]

III. Results and discussion

Following the outlined procedure above, the photodynamics of the p-DTS(PTTh$_2$)$_2$ molecule (Fig. 1(a)) have been studied using the NA-ESMD simulations. The molecule is initially excited to the broad high-energy band in the 3–4 eV range. After that, the internal conversion to the lowest S$_1$ state has been analyzed. The experimental[54] and simulated absorption and emission spectra are displayed in Fig. 1(b). Compared to the experiment, the calculated spectrum is blue-shifted by $\sim$0.34 eV, which may be attributed to solvent effects absent in the simulations. This is

consistent with our previous computational investigation of p-DTS(PTTh$_2$)$_2$ molecules using the TDDFT approach and the polarizable continuum model[54] suggesting that the absorption spectra undergo $\sim$0.2–0.3 eV solvatochromic red-shifts depending on the solvent polarity. Notably, adding an implicit solvent does not lead to any noticeable reordering of the excited states in the 2–4 eV spectral region apart from systematic solvatochromic shifts across the entire spectrum.[54] Otherwise, good agreement between theory and experiment is achieved for the relative energies between the lowest S$_0$–S$_1$ peak and the broad high-energy band in the 3–4 eV range. Moreover, the calculated emission spectrum presents a larger Stokes shift than the reported experimental data. Such an overestimate of the Stoke shift is typical for electronic structure methodologies using unscreened (100%) orbital exchange, such as long-range corrected DFT models.[54] Individual contributions of different excited states to the absorption spectrum are analyzed in Fig. S1(a)–(e) (ESI†). As can be seen, 40 excited states are necessary in order to reproduce the high-energy band of the spectrum. In agreement with previous ab $initio$ calculations,[54] Fig. S1(a) (ESI†) shows that the strong low-energy peak at 2.2 eV corresponds uniquely to the lowest S$_0$–S$_1$ optically active band-gap transition. Furthermore, the observed shoulder on the blue side of the fundamental S$_0$–S$_1$ peak can be mainly attributed to the second lowest singlet S$_2$ state (Fig. S1(b) (ESI†)). Finally, Fig. S1(b)–(e) (ESI†) indicate that this high-energy band is associated with multiple excited states.

We further explore the polarization of the different excitations that contribute to the absorption spectrum of the p-DTS(PTTh$_2$)$_2$ molecule. For this analysis, each initially stored ground state configuration has been translated to a body fixed reference frame with origin in its corresponding center of mass. Then, the mutually orthogonal principal axes of rotation (a, b, c) of the rigid body are obtained from the eigenvectors of the moment of inertia tensor. The first moment of inertia a is oriented mainly along the long axis of the molecule, and the molecular plane corresponds to the plane formed by the a- and b-axes. As an example, Fig. 1(a) displays the AM1 optimized structure of p-DTS(PTTh$_2$)$_2$ oriented along its principal inertial axes. Thereafter, the Cartesian coordinate axes of each snapshot ground-state configuration are reoriented so they coincide with their corresponding principal axes of rotation. Within this new body fixed reference frame, we further calculate the transition dipole moments. Fig. 2(a)–(c) show the contributions of the different excited states to the resulting intensity of the polarized absorption spectra in the directions parallel to the a-, b- an c-inertial axes, respectively. While the transition dipole moment of the S$_1$ state is polarized along the first a-inertial axes, the corresponding transition to the S$_2$ state is mostly parallel to the second b-inertial axes. In contrast, the states contributing to the higher-energy peak have various polarizations rarely aligned with the inertial axes of the molecule.

The initial excited states for the NA-ESMD modeling are populated according to their contributions to the simulated absorption spectrum shown in Fig. S1 (ESI†) using a Frank–Condon window defined by a Gaussian shaped laser centered at 3.65 eV with a FWHM of 100 fs. The resulting final distribution
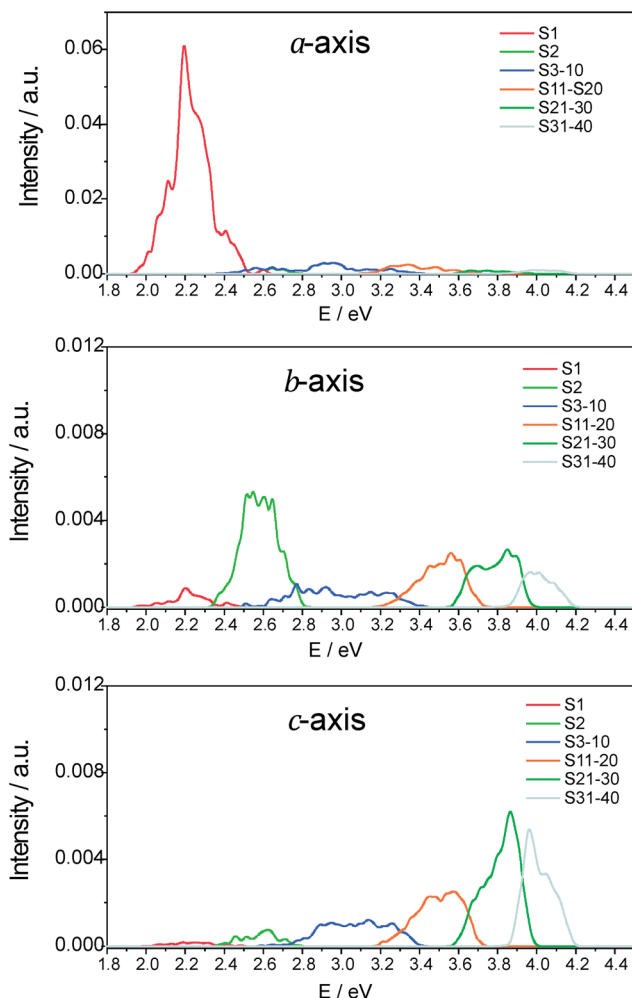
Paper

Fig. 2 (a–c) Relative absorbance intensities in the directions parallel to the a-, b- an c-inertial axes of the p-DTS(PTTh$_2$)$_2$ molecule.
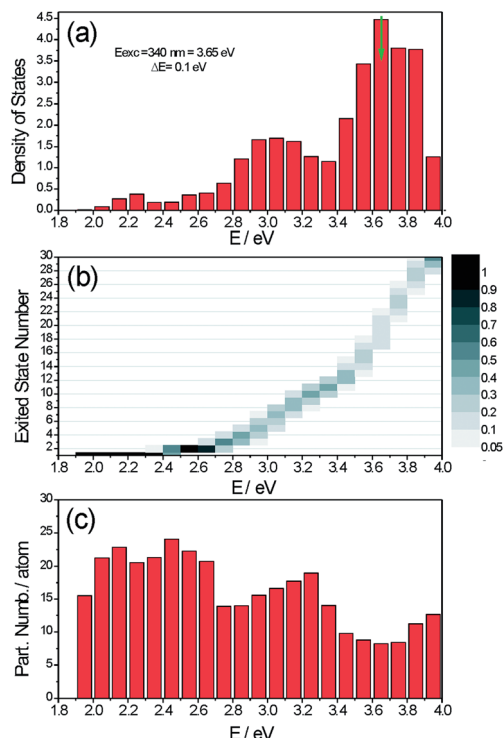

Fig. 3 (a) Density of excited states. The arrow indicates the maximum of the laser excitation energy used in the simulations. (b) Contribution of the different adiabatic electronic states to the density of states within energy intervals of 0.1 eV. (c) Atomic participation number for the transition densities of electronic states at the different energy intervals.

of initial states is broad and asymmetric spanning the S_{13}–S_{30} state range as shown in Fig. S2 (ESI).† All contributing states have small individual oscillator strengths and various polarizations (Fig. S1(c) in the ESI,† and 2(a)–(c)).

The density of electronic states has an impact not only on the distribution of initial states but also on the transient stabilization of the different intermediate excited electronic states throughout the relaxation dynamics. Therefore, in Fig. 3(a), the average over all the initial configurations of the density of excited states is depicted in different wavelength ranges. For the sake of completeness, Fig. 3(b) shows the average contribution of the different adiabatic electronic states to the density of states within an energy interval of 0.1 eV. The larger density of states is observed at the excitation wavelength that corresponds to the middle of the broad high-energy band of the molecule. The density of states decreases towards the red side of this band presenting a minimum at ~3.3 eV that corresponds to the peak of the S_{11} state (see Fig. 3(b) and S1(c) (ESI†)). Thereafter, a new increase in the density of states is observed in the middle range between ~2.9 eV and 3.2 eV. Finally, energies lower than ~2.7 eV can be associated only with the S_2 and S_1 states (see

Fig. 3(b) and S1(b) (ESI†)). In order to further characterize spatial localization properties of different excited states, we have evaluated the atomic participation number, $P_{at}(t)$, (eqn (2)) for the transition densities of electronic states at the different energy intervals. The results are shown in Fig. 3(c). Overall, the value of $P_{at}(t)$ decreases when moving from the low- to high-excitation energies. This indicates that the low-energy states have extended conjugation and are mostly delocalized across the entire molecule, whereas the high-energy states are essentially localized. An exception is observed at ~3.3 eV corresponding to the peak of the S_{11} state, which is delocalized as well.

Fig. 4 details the average populations of different electronic excited states as a function of time. During the internal conversion processes among a dense manifold of excited states, dynamics of population and depopulation of individual states (which are consecutive in energy order) frequently show similar behavior (e.g., compare curves in Fig. 4(c)–(e)). This is likely a consequence of an average over many trajectories with a rapid interchange of electronic population. The latter occurs due to large non-adiabatic couplings related to small energy gaps ΔE between states (according to the Hellmann–Feynman theorem, the non-adiabatic coupling scales as $1/\Delta E$). In particular, the initially populated S_{30} to S_{13} high-energy excited states (Fig. 4(e) and (f)) experience an ultrafast relaxation via internal conversion in ~70 fs without an effective transient accumulation of

This journal is © The Royal Society of Chemistry 2014

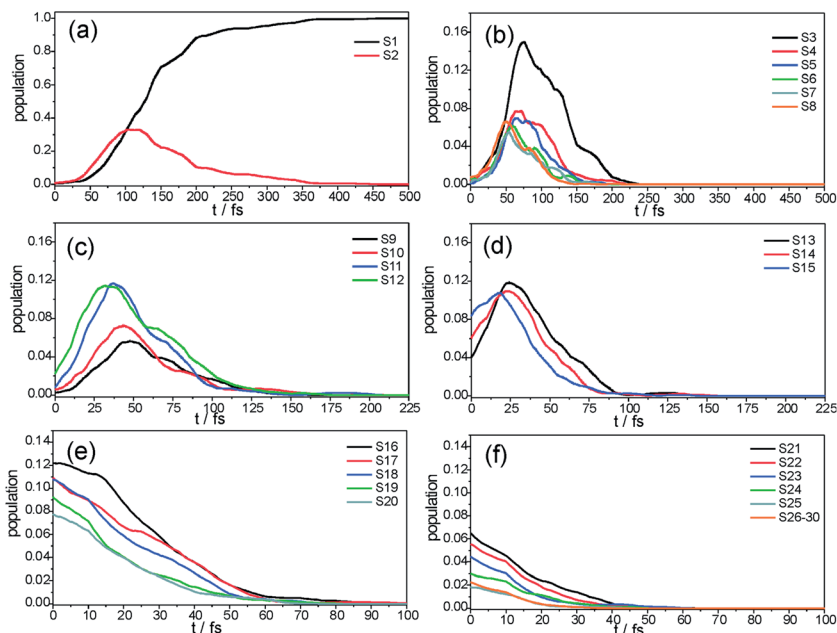Energy Environ. Sci., 2014, 7, 1175–1184 | 1179

Fig. 4   Population of each electronic surface as a function of time obtained from the fraction of trajectories in each state.

their initial excess of energy. According to Fig. S1(c) and (d) (ESI†), these states absorb most of their initial excess of energy in the range of 3.6 to 3.9 eV. This range of the spectrum presents a high density of states (Fig. 3(a)) that likely contributes to the high efficient internal conversion of these states. In contrast, Fig. 4(d) shows that the absorbing states from S_{15} to S_{13}, in the range of ∼3.5–3.6 eV, accumulate their excess of energy that reach maximum values at 25 fs, indicating that the rates at which they receive population from the high-energy states exceed the rates at which they are capable of relaxing. This is consistent with the gradual decreases in the density of states in this range of the spectrum. Thereafter, the populations of the middle-range intermediate states, from S_{12} to S_2, evolve in time reaching their corresponding maximum values at gradually increasing times. It is also interesting to note that the maximum values reached by the populations of states S_{12}–S_{11} are at least 50% higher than the corresponding maximum values reached by the populations of the S_9–S_4 states. These variations in the maximum values of the transient populations can be associated with changes in the density of states along the relaxation process. Furthermore, Fig. 4(a) and (b) show that the transient accumulation of populations achieved by S_3 and S_2 states is significantly larger and their relaxation rates are slower than the other states. Finally, the ultrafast internal conversion to the lowest S_1 excited state is achieved with an efficiency of 100% on a timescale of about 200 fs.

Let us analyze now the efficient internal conversion mechanism that leads to the complete decay of the photoexcited molecule to its lowest S_1 excited state. According to the MDQT method, electronic transitions during the NA-ESMD are represented as hops from one initial electronic state S_i to another S_f final state. Fig. 5(a) represents the relative probabilities of effective $S_i \rightarrow S_f$ transitions during all the NA-ESMD simulations. The relative probabilities have been normalized for hops
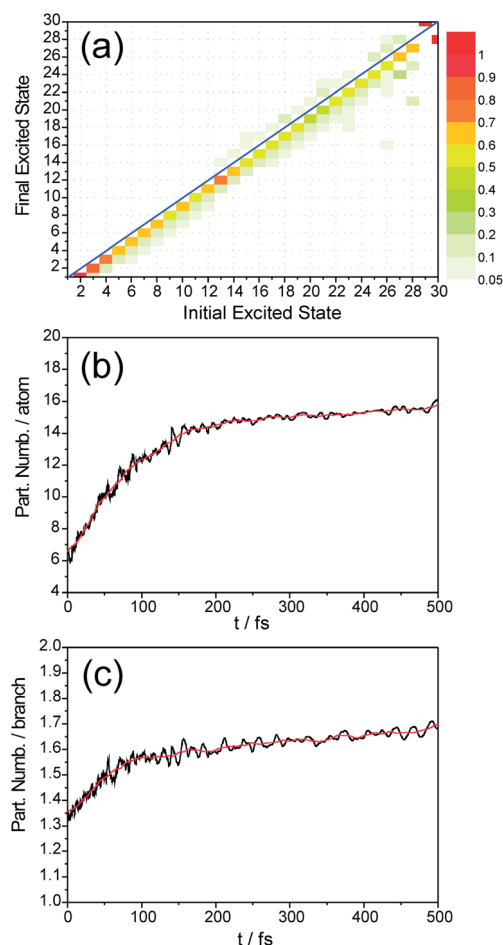

Fig. 5   (a) Distribution of the number of effective $S_i \rightarrow S_f$ hops during all the NA-ESMD simulations. The relative probabilities are normalized for hops corresponding to the same S_i state. Time-dependence of (b) the average atomic participation number and (c) the average branch participation number.

corresponding to the same S_i state. An effective $S_i \rightarrow S_f$ transition refers to $S_i \rightarrow S_f$ hops for which no backhopping $S_f \rightarrow S_i$ occurs along the rest of the trajectory. As can be seen, the $S_i \rightarrow S_{i-1}$ hops are the most frequent electronic transitions. This is more evident for the intermediate states S_{12}, S_{13}, and S_{14} that belong to a low-density of states region of the spectrum and, therefore, have large energy gaps between states. Therefore, the radiationless deactivation, from the initial bunch of that involves electronic transitions between the transient current state to the corresponding state directly below in energy.

A further characterization of the internal conversion of the photoexcited p-DTS(PTTh$_2$)$_2$ molecule can be achieved by analyzing the evolution in time of the atomic and branch average participation number, $P_{at}(t)$ and $P_{branch}(t)$, as shown in Fig. 5(b) and (c), respectively. We observe that both the atomic and branch delocalization of states steadily increase in time, indicating the extent of the conjugation and wavefunction delocalization during the relaxation process. Particularly, the initial fast branch delocalization involves transition from the branch-localized S_{12} state to the delocalized S_{12} state (see Fig. 7). These states belong to the middle energy-range ($\sim$3.3 eV) of the absorption spectra and their populations reach maximum values at $\sim$30 fs. According to Fig. 5(c), the branch participation number $P_{branch}(t)$ rapidly increases during this time. Therefore, $S_{12} \rightarrow S_{11}$ transitions can be considered as the main contribution to the initial fast delocalization of states between the two branches. A more detailed interpretation of the $P_{at}(t)$ behavior

can be obtained by decomposing the electronic transition density in contributions from the different moieties of the p-DTS(PTTh$_2$)$_2$ molecule (eqn (1)). Consequently, the intramolecular electronic energy redistribution that takes place during the internal conversion process can be followed. Fig. 6 shows the time-dependent average of the fraction of the transition density localized on the DTS, Th$_2$, and PT units (see Fig. 1(a)). We observe an effective redistribution of the wavefunction from the donor Th$_2$ to the acceptor PT moieties, while the value on the donor DTS presents a slight increase at longer times (Fig. 6(a)). Between the two aromatic rings of the PT moiety, PTb is the one whose transition density increases the most during the non-radiative process, while the PTa ring only presents a small transient increase at short time (Fig. 6(b)). In contrast, both Th$_2$ units seem to equally release the electronic energy initially localized on them by photoexcitation (Fig. 6(c)).

As an illustration, Fig. 7 displays the p-DTS(PTTh$_2$)$_2$ molecule with the snapshots of the distribution of the electronic transition density at different times during a typical NA-ESMD photoexcited trajectory. The initial photoexcited state is actually a superposition of several high-energy states (see Fig. S2 (ESI†)), S_{18} being the one that contributes the most. As shown in Fig. 5(c), the transition density of the initial excited state is asymmetrically delocalized between the two equivalent branches of the p-DTS(PTTh$_2$)$_2$ molecule. Then, according to Fig. 4(d), the transient peaks of electronic populations for states absorbed in the range of $\sim$3.5–3.6 eV are observed at $\sim$25 fs. At that time, the transition density is not yet delocalized between the two branches, and the transient partial localization of the transition density on the PTa ring takes place. After that, the populations of the middle-range intermediate states, from S_{12} to S_2, evolve in time reaching their corresponding maximum values at gradually increasing times. At $\sim$40 fs (see Fig. 4(c)) the population of the S_{12} and S_{11} states reaches its maximum value and, according to Fig. 3, the system crosses a region of low density of states fully delocalized across the molecule. This induces the transient population to be trapped at these intermediate states. Finally, at $\sim$100 fs the electronic population of S_2 reaches its maximum value (see Fig. 4(a)) and, thereafter, the system completely relaxes to the lowest S_1 state.

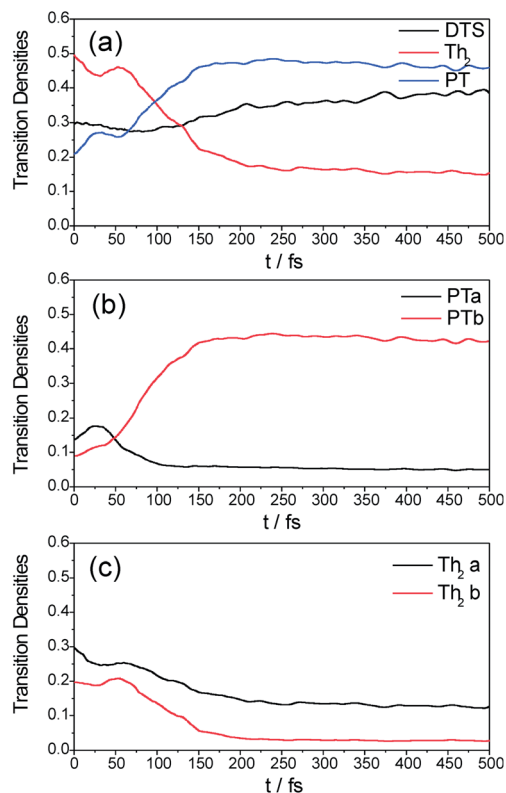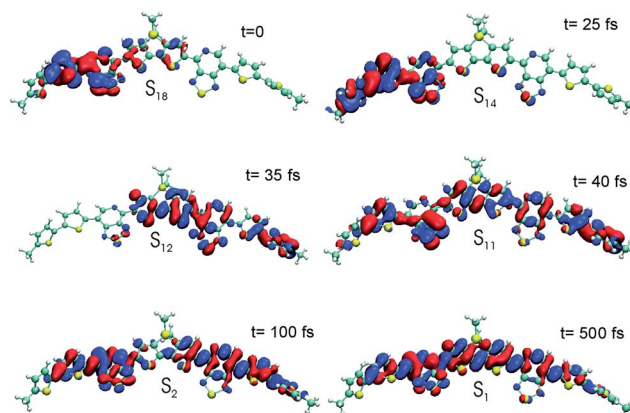

Fig. 6 Time-dependent average of the fraction of the transition density localized at the different units of the p-DTS(PTTh$_2$)$_2$: (a) DTS, Th$_2$, and PT, (b) PTa and PTb, and (c) Th$_2$a and Th$_2$b.

Fig. 7 Localization of the electronic transition density at different times along the representative trajectory in the NA-ESMD simulations.

This journal is © The Royal Society of Chemistry 2014

Energy Environ. Sci., 2014, **7**, 1175–1184 | **1181**

It is interesting to note that the electronic transition density for the S_1 state is significantly localized on the DTS moiety (particularly in the S_1 vibrationally relaxed conformation).[54] Therefore, a slight increase of the average fraction of transition density localized on the DTS is observed at the end of the internal conversion process (see Fig. 6(a)). We have also analyzed the spatial distribution of the electronic transition density of the S_1 state at different times during the NA-ESMD simulations. The results are depicted in Fig. S3 (ESI†). Localization of the transition density associated with this state does not change significantly during the non-adiabatic molecular dynamics simulation. The same behavior is expected for other excited electronic states. This suggests that the reported intramolecular electronic energy redistribution occurs due to nonadiabatic dynamics involving multiple excited states during the non-radiative relaxation process.

The direction of the non-adiabatic coupling vector $\mathbf{d}_{\alpha\beta}$ between the α and β electronic excited states corresponds to the direction of nuclear motions activated in the inter-state energy transfer during internal conversion.[66,75–78] Therefore, in order to explore the role of vibrational dynamics in the intramolecular energy redistribution, Fig. 8 depicts non-adiabatic coupling vectors $\mathbf{d}_{\alpha\beta}$ for a typical trajectory at times of quantum transitions. According to the sequential mechanism of radiationless deactivation, previously discussed in Fig. 5(a), only $S_i \rightarrow S_{i-1}$ transitions are analyzed. Comparison with Fig. 7 indicates that the observed intramolecular vibrational energy redistribution is concomitant with the electronic wavefunction delocalization throughout the entire internal conversion process. The initial vibrational and electronic energy redistribution is asymmetrically delocalized between the two equivalent branches of the p-DTS(PTTh$_2$)$_2$ molecule. This can be observed in the direction of inter-state electronic transition $S_{18} \rightarrow S_{17}$, taken as a representative example of hops involving the initial manifold of high-energy excited states (see Fig. S2 (ESI†)). The molecular motions that couple these states involve concerted motions of donor Th$_2$ (a and b) and acceptor PT moieties. The initial effective redistribution of the wavefunction from the donor Th$_2$ to the acceptor PT moieties (shown in Fig. 6) provides an electronic footprint of this process. Subsequent electronic transitions involving middle-range intermediate states as $S_{15} \rightarrow S_{14}$ and $S_{12} \rightarrow S_{11}$ lead to the progressive delocalization of the electronic wavefunctions between the two branches of the p-DTS(PTTh$_2$)$_2$ molecule. Finally, $S_3 \rightarrow S_2$ and $S_2 \rightarrow S_1$ transitions take place due to nuclear motions distributed between PT and DTS moieties. Thereby, the distribution of the atomic displacement involved in each non-adiabatic coupling vector $\mathbf{d}_{\alpha\beta}$ reveals their roles as "bridges" through which an efficient internal conversion takes place. Notably, none of the nonadiabatic coupling vectors $\mathbf{d}_{\alpha\beta}$ displayed in Fig. 8 can be associated with the ground state vibrational normal modes as established by our previous study.[89] Instead, these pictures represent specific unique nuclear displacements related only to the nature of two electronic states involved in the dynamics. Such displacements activated during excited state dynamics provide interesting complementary information for recent studies[90] of nonbonding interactions often incorporated into conformational "locking" schemes for similar classes of molecules.

IV. Conclusions

Ultrafast internal conversion to the lowest excited state in the recently synthesized molecular donor p-DTS(PTTh$_2$)$_2$ has been computationally investigated. Our NA-ESMD modeling provided detailed information on the intramolecular vibrational energy redistribution and relaxation of the excess of electronic energy after photoexcitation to the broad high-energy band in the 3–4 eV range. Observed efficient radiationless deactivation takes place mainly through a sequential mechanism involving electronic transitions between the current transient state and the corresponding state directly below in energy. During its electronic relaxation, the photoinduced wavepacket samples regions of the absorption with varying density of states. Changes in the density of states impact the maximum values and time-dependence of the accumulated populations of the different intermediate excited electronic states. Regions of relatively low density induce the transient population trapping at intermediate electronic states. The intramolecular electronic energy redistribution that takes place during the internal conversion has been further analyzed in terms of the spatial distribution of the time-dependent electronic wavefunction. Our analysis reveals an effective redistribution of the transition density from the donor Th$_2$ to the acceptor PT moieties, without significant changes in the fraction of the transition density localized on the DTS moiety. Overall, the delocalization of the wavefunction steadily increases as electronic populations migrate to the lower-energy states. Notably, in our modeling of internal conversion, about 1–2 eV electronic energy is being deposited into vibrational degrees of freedom on a hundred femtosecond timescale, leading to rapid heating of the p-DTS(PTTh$_2$)$_2$ molecule. Nevertheless, none of the trajectories resulted in a bond-breaking or decomposition of the system. This suggests that the possibility of intra-molecular photodamage after photoexcitation to high-energy states in the 3–4 eV region is limited. We believe that providing a detailed understanding of the complex electronic dynamics in this molecule is a critical step for future
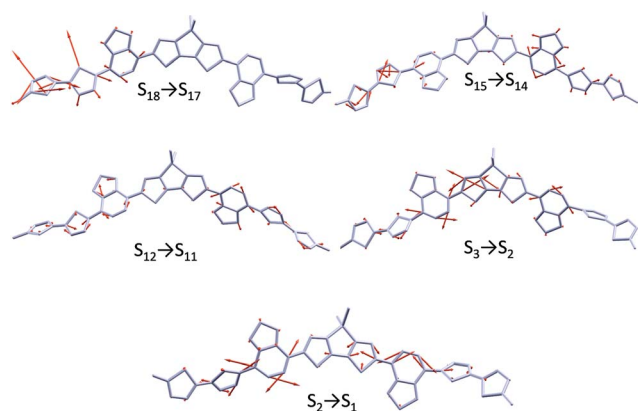

Fig. 8 Non-adiabatic coupling vectors $\mathbf{d}_{\alpha\beta}$ for a typical trajectory at selected quantum transitions $S_i \rightarrow S_{i-1}$.

1182 | Energy Environ. Sci., 2014, 7, 1175–1184

This journal is © The Royal Society of Chemistry 2014

improvements of its exceptional light-harvesting and donor capabilities in BHJ solar cells.[53]

While simulated intramolecular excited state dynamics constitutes a dominating primary relaxation step in the photo-excited material (*e.g.*, solar cells) followed by the exciton transport step, detailed fully atomistic simulations of non-adiabatic dynamics are necessary to address the existence of other possible photoinduced processes and pathways that may arise due to interactions of the *p*-DTS(PTTh$_2$)$_2$ donor with the surrounding polar solvent (*e.g.*, hydrogen bonding) or with neighboring *p*-DTS(PTTh$_2$)$_2$ molecules in a crystal or an amorphous phase.[53,54] For example, it has been demonstrated that the solvent effects like hydrogen bonding interactions can remarkably influence the ultrafast excited-state processes like internal conversion, intramolecular charge transfer, and photoinduced electron transfer in a variety of molecular systems.[91–93] Such simulations can potentially be performed utilizing the Quantum Mechanics/Molecular Mechanics (QM/MM) framework,[94–97] which will be a subject of our future studies.

Acknowledgements

References

1 C. Li, M. Liu, N. G. Pschirer, M. Baumgarten and K. Müllen, *Chem. Rev.*, 2010, **110**, 6817–6855.

2 S. Günes, H. Neugebauer and N. S. Sariciftci, *Chem. Rev.*, 2007, **107**, 1324–1338.

3 *Organic photovoltaics: materials, device physics, and manufacturing technologies*, ed. U. Brabec, C. J. Dyakonov and V. Scherf, WILEY-VCH, Weinheim, 2008.

4 J. D. Servaites, M. a. Ratner and T. J. Marks, *Energy Environ. Sci.*, 2011, **4**, 4410–4422.

5 B. Kippelen and J.-L. Brédas, *Energy Environ. Sci.*, 2009, **2**, 251–261.

6 O. Inganäs, F. Zhang, K. Tvingstedt, L. M. Andersson, S. Hellström and M. R. Andersson, *Adv. Mater.*, 2010, **22**, E100–E116.

7 J. L. Brédas, J. E. Norton, J. Cornil and V. Coropceanu, *Acc. Chem. Res.*, 2009, **42**, 1691–1699.

8 A. J. Heeger, *Chem. Soc. Rev.*, 2010, **39**, 2354–2371.

9 R. F. Service, *Science*, 2011, **332**, 239.

10 L.-M. Chen, Z. Hong, G. Li and Y. Yang, *Adv. Mater.*, 2009, **21**, 1434–1449.

11 C. J. Brabec, S. Gowrisanker, J. J. M. Halls, D. Laird, S. Jia and S. P. Williams, *Adv. Mater.*, 2010, **22**, 3839–3856.

12 G. Yu, J. Gao, J. C. Hummelen, F. Wudl and A. J. Heeger, *Science*, 1995, **270**, 1789–1791.

13 G. Dennler, M. C. Scharber and C. J. Brabec, *Adv. Mater.*, 2009, **21**, 1323–1338.

14 Y.-J. Cheng, S.-H. Yang and C.-S. Hsu, *Chem. Rev.*, 2009, **109**, 5868–5923.

15 M. C. Scharber, D. Mühlbacher, M. Koppe, P. Denk, C. Waldauf, A. J. Heeger and C. J. Brabec, *Adv. Mater.*, 2006, **18**, 789–794.

16 Y. Liang, Z. Xu, J. Xia, S.-T. Tsai, Y. Wu, G. Li, C. Ray and L. Yu, *Adv. Mater.*, 2010, **22**, E135–E138.

17 D. Gendron and M. Leclerc, *Energy Environ. Sci.*, 2011, **4**, 1225–1237.

18 E. J. Luber and J. M. Buriak, *ACS Nano*, 2013, **7**, 4708–4714.

19 http://www.nrel.gov/ncpv/images/efficiency_chart.jpg.

20 W. Ma, C. Yang, X. Gong, K. Lee and A. J. Heeger, *Adv. Funct. Mater.*, 2005, **15**, 1617–1622.

21 M. A. Green, K. Emery, Y. Hishikawa and W. Warta, *Prog. Photovoltaics*, 2011, **19**, 84–92.

22 J. Y. Kim, S. H. Kim, H.-H. Lee, K. Lee, W. Ma, X. Gong and A. J. Heeger, *Adv. Mater.*, 2006, **18**, 572–576.

23 J. Peet, J. Y. Kim, N. E. Coates, W. L. Ma, D. Moses, A. J. Heeger and G. C. Bazan, *Nat. Mater.*, 2007, **6**, 497–500.

24 J. Y. Kim, K. Lee, N. E. Coates, D. Moses, T.-Q. Nguyen, M. Dante and A. J. Heeger, *Science*, 2007, **317**, 222–225.

25 R. Gaudiana and C. J. Brabec, *Nat. Photonics*, 2008, **2**, 287–289.

26 M. A. Green, K. Emery, Y. Hishikawa, W. Warta and E. D. Dunlop, *Prog. Photovoltaics*, 2013, **21**, 1–11.

27 B. Walker, C. Kim and T.-Q. Nguyen, *Chem. Mater.*, 2011, **23**, 470–482.

28 Y. Lin, Y. Li and X. Zhan, *Chem. Soc. Rev.*, 2012, **41**, 4245–4272.

29 A. Mishra and P. Bäuerle, *Angew. Chem., Int. Ed.*, 2012, **51**, 2020–2067.

30 J. Roncali, *Acc. Chem. Res.*, 2009, **42**, 1719–1730.

31 M. T. Lloyd, J. E. Anthony and G. G. Malliaras, *Mater. Today*, 2007, **10**, 34–41.

32 Y. Liu, X. Wan, B. Yin, J. Zhou, G. Long, S. Yin and Y. Chen, *J. Mater. Chem.*, 2010, **20**, 2464–2468.

33 B. Yin, L. Yang, Y. Liu, Y. Chen, Q. Qi, F. Zhang and S. Yin, *Appl. Phys. Lett.*, 2010, **97**, 023303–023305.

34 H. Fan, H. Shang, Y. Li and X. Zhan, *Appl. Phys. Lett.*, 2010, **97**, 133302.

35 J. Zhang, D. Deng, C. He, Y. He, M. Zhang, Z.-G. Zhang, Z. Zhang and Y. Li, *Chem. Mater.*, 2011, **23**, 817–822.

36 H. Shang, H. Fan, Y. Liu, W. Hu, Y. Li and X. Zhan, *Adv. Mater.*, 2011, **23**, 1554–1557.

37 O. D. Jurchescu, J. Baas and T. T. M. Palstra, *Appl. Phys. Lett.*, 2004, **84**, 3061.

38 O. Ostroverkhova, S. Shcherbyna, D. G. Cooke, R. F. Egerton, F. A. Hegmann, R. R. Tykwinski, S. R. Parkin and J. E. Anthony, *J. Appl. Phys.*, 2005, **98**, 033701–033712.

39 V. C. Sundar, J. Zaumseil, V. Podzorov, E. Menard, R. L. Willett, T. Someya, M. E. Gershenson and J. a. Rogers, *Science*, 2004, **303**, 1644–1646.

40 J. E. Anthony and B. Purushothaman, *Proc. SPIE 6658, Organic Field-Effect Transistors VI*, 2007, vol. 6658, p. 66580L.

41 B. Walker, A. B. Tamayo, X.-D. Dang, P. Zalar, J. H. Seo, A. Garcia, M. Tantiwiwat and T.-Q. Nguyen, *Adv. Funct. Mater.*, 2009, **19**, 3063–3069.

42 H. M. Ko, H. Choi, S. Paek, K. Kim, K. Song, J. K. Lee and J. Ko, *J. Mater. Chem.*, 2011, **21**, 7248–7253.

43 G. Wei, S. Wang, K. Renshaw, M. E. Thompson and S. R. Forrest, *ACS Nano*, 2010, **4**, 1927–1934.

44 D. Bagnis, L. Beverina, H. Huang, F. Silvestri, Y. Yao, H. Yan, G. a. Pagani, T. J. Marks and A. Facchetti, *J. Am.Chem. Soc.*, 2010, **132**, 4074–4075.

45 H. Bürckstümmer, N. M. Kronenberg, M. Gsänger, M. Stolte, K. Meerholz and F. Würthner, *J. Mater. Chem.*, 2010, **20**, 240–243.

46 H. Bürckstümmer, N. M. Kronenberg, K. Meerholz and F. Würthner, *Org. Lett.*, 2010, **12**, 3666–3669.

47 G. C. Welch, L. a. Perez, C. V. Hoven, Y. Zhang, X.-D. Dang, A. Sharenko, M. F. Toney, E. J. Kramer, T.-Q. Nguyen and G. C. Bazan, *J. Mater. Chem.*, 2011, **21**, 12700–12709.

48 H. Meier, *Angew. Chem., Int. Ed.*, 2005, **44**, 2482–2506.

49 J. Roncali, *Chem. Rev.*, 1997, **97**, 173–206.

50 G. C. Welch, R. Coffin, J. Peet and G. C. Bazan, *J. Am. Chem. Soc.*, 2009, **131**, 10802–10803.

51 B. P. Karsten, J. C. Bijleveld, L. Viani, J. Cornil, J. Gierschner and R. a. J. Janssen, *J. Mater. Chem.*, 2009, **19**, 5343–5350.

52 B. P. Karsten, L. Viani, J. Gierschner, J. Cornil and R. a. J. Janssen, *J. Phys. Chem. A*, 2008, **112**, 10764–10773.

53 Y. Sun, G. C. Welch, W. L. Leong, C. J. Takacs, G. C. Bazan and A. J. Heeger, *Nat. Mater.*, 2012, **11**, 44–48.

54 A. Zhugayevych, O. Postupna, G. C. Welch, G. C. Bazan and S. Tretiak, *J. Phys. Chem. C*, 2013, **117**, 4920–4930.

55 J. Clark, T. Nelson, S. Tretiak, G. Cirmi and G. Lanzani, *Nat. Phys.*, 2012, **8**, 225–231.

56 T. Nelson, S. Fernandez-Aberti, V. Chernyak, A. E. Roitberg and S. Tretiak, *J. Phys. Chem. B*, 2011, **115**, 5402–5414.

57 T. Nelson, S. Fernandez-Aberti, V. Chernyak, A. E. Roitberg and S. Tretiak, *J. Chem. Phys.*, 2012, **136**, 054108–054120.

58 S. Fernandez-Aberti, V. D. Kleiman, S. Tretiak and A. E. Roitberg, *J. Phys. Chem. A*, 2009, **113**, 7535–7542.

59 S. Fernandez-Aberti, V. D. Kleiman, S. Tretiak and A. E. Roitberg, *J. Phys. Chem. Lett.*, 2010, **1**, 2699–2704.

60 S. Fernandez-Aberti, A. E. Roitberg, V. D. Kleiman, T. Nelson and S. Tretiak, *J. Chem. Phys.*, 2012, **137**, 22A526–22A535.

61 S. Tretiak, A. Saxena, R. L. Martin and A. R. Bishop, *Chem. Phys. Lett.*, 2000, **331**, 561–568.

62 S. Tretiak, A. Saxena, R. L. Martin and A. R. Bishop, *Proc. Natl. Acad. Sci. U. S. A.*, 2003, **100**, 2185–2190.

63 G. A. Worth, M. A. Robb and B. Lasorne, *Mol. Phys.*, 2008, **106**, 2077–2091.

64 J. C. Tully, *J. Chem. Phys.*, 1990, **93**, 1061–1071.

65 S. Hammes-Schiffer and J. C. Tully, *J. Chem. Phys.*, 1994, **101**, 4657–4667.

66 J. C. Tully, *Int. J. Quantum Chem.*, 1991, **40**, 299–309.

67 S. Tretiak and S. Mukamel, *Chem. Rev.*, 2002, **102**, 3171–3212.

68 V. Chernyak, M. F. Schulz, S. Mukamel, S. Tretiak and E. V. Tsiper, *J. Chem. Phys.*, 2000, **113**, 36.

69 S. Tretiak, C. M. Isborn, A. M. N. Niklasson and M. Challacombe, *J. Chem. Phys.*, 2009, **130**, 054111–054127.

70 F. Furche and R. Ahlrichs, *J. Chem. Phys.*, 2002, **117**, 7433–7448.

71 S. Tretiak and V. Chernyak, *J. Chem. Phys.*, 2003, **119**, 8809–8823.

72 M. Tommasini, V. Chernyak and S. Mukamel, *Int. J. Quantum Chem.*, 2001, **85**, 225–238.

73 V. Chernyak and S. Mukamel, *J. Chem. Phys.*, 2000, **8**, 3572–3579.

74 R. Send and F. Furche, *J. Chem. Phys.*, 2010, **132**, 044107–044119.

75 P. Pechukas, *Phys. Rev.*, 1969, **181**, 166–174.

76 F. Webster, P. J. Rossky and R. A. Friesner, *Comput. Phys. Commun.*, 1991, **63**, 494–552.

77 F. Webster, J. Schnitker, M. S. Friedrichs, R. A. Friesner and P. J. Rossky, *Phys. Rev. Lett.*, 1991, **66**, 3172–3175.

78 D. F. Coker and L. Xiao, *J. Chem. Phys.*, 1995, **102**, 496–510.

79 S. Mukamel, *Nature*, 1997, **388**, 425–427.

80 S. Mukamel, S. Tretiak, T. Wagersreiter and V. Chernyak, *Science*, 1997, **277**, 781–787.

81 S. Tretiak, V. Chernyak and S. Mukamel, *J. Chem. Phys.*, 1996, **105**, 8914–8928.

82 S. Tretiak, W. M. Zhang, V. Chernyak and S. Mukamel, *Proc. Natl. Acad. Sci. U. S. A.*, 1999, **96**, 13003–13008.

83 M. J. S. Dewar, E. G. Zoebisch, E. F. Healy and J. J. P. Stewart, *J. Am. Chem. Soc.*, 1985, **107**, 3902–3909.

84 S. Tretiak, V. Chernyak and S. Mukamel, *J. Am. Chem. Soc.*, 1997, **119**, 11408–11419.

85 S. Tretiak, V. Chernyak and S. Mukamel, *Chem. Phys. Lett.*, 1996, **259**, 55–61.

86 C. Wu, S. V. Malinin, S. Tretiak and V. Y. Chernyak, *Nat. Phys.*, 2006, **2**, 631–635.

87 R. J. Bell, P. Dean and D. C. Hibbins-Butler, *J. Phys. C: Solid State Phys.*, 1970, **3**, 2111–2118.

88 S. N. Taraskin and S. R. Elliott, *Phys. Rev. B: Condens. Matter Mater. Phys.*, 1999, **59**, 8572–8585.

89 M. a. Soler, A. E. Roitberg, T. Nelson, S. Tretiak and S. Fernandez-Aberti, *J. Phys. Chem. A*, 2012, **116**, 9802–9810.

90 N. E. Jackson, B. M. Savoie, K. L. Kohlstedt, M. Olvera de la Cruz, G. C. Schatz, L. X. Chen and M. a. Ratner, *J. Am. Chem. Soc.*, 2013, **135**, 10475–10483.

91 G.-J. Zhao and K.-L. Han, *Acc. Chem. Res.*, 2012, **45**, 404–413.

92 G.-J. Zhao and K.-L. Han, *J. Phys. Chem. A*, 2007, **111**, 9218–9223.

93 G.-J. Zhao, J.-Y. Liu, L.-C. Zhou and K.-L. Han, *J. Phys. Chem. B*, 2007, **111**, 8940–8945.

94 A. Warshel and M. Levitt, *J. Mol. Biol.*, 1976, **103**, 227–249.

95 M. J. Field, P. A. Bash and M. Karplus, *J. Comput. Chem.*, 1990, **11**, 700–733.

96 H. Lin and D. G. Truhlar, *Theor. Chem. Acc.*, 2007, **117**, 185–199.

97 H. M. Senn and W. Thiel, in *Atomistic Approaches in Modern Biology, Top. Curr. Chem.*, ed. M. Reiher, Springer, Berlin, 2007, vol. 268, pp. 173–290.